Supporting Information

Axial optimization of biomimetic nanoenzymes catalysts applied to oxygen reduction reactions

Jingjing Liu,[#,a] Jingjing Jia,[#,b] Huiying Wen,[#,a] Siqi Li,[a] Yingjie Wu,[a] Qi Wang,[a] Ziwang Kan,[a] Yan Li,[a] Xia Wu,[a] Jingxiang Zhao[,b] Song Liu,[*,a] Bin Li,[*,a]*

a College of Chemistry, Chemical Engineering and Resource Utilization, Northeast Forestry University, Harbin 150040, China

b College of Chemistry and Chemical Engineering, and Key Laboratory of Photonic and Electronic Bandgap Materials, Ministry of Education, Harbin Normal University, Harbin, 150025, China

To whom correspondence should be addressed. Email: zhaojingxiang@hrbnu.edu.cn (J. Zhao), carlosliusong@nefu.edu.cn (S. Liu) and libinzh62@163.com (B. Li).

 # Jingjing Liu, Jingjing Jia and Huiying Wen contribute equally to this work.

Computational Details:

The spin-polarized density functional theory (DFT) calculations within the Vienna Ab initio Simulation Package (VASP)[1,2] were carried out to obtain the stable configurations, energies, and the correspondingelectronic properties. We employed the projector-augmented plane wave (PAW)[3,4] method to treat the ion-electron interaction. The generalized gradient approximation (GGA) in the form of Perdew−Burke−Ernzerhof (PBE) exchange-correlation functional[5] was adopted to obtain the electronic properties, including band structures and density of states. A kinetic energy cutoff of 500 eV was adopted, and the convergence criteria for the total energy and the atomic force were set to be 10^{-5} eV and 10^{-4} eV/Å, respectively. During the geometry relaxation, a 5 × 5 × 1 Γ-centered Monkhorst−Pack kpoint grid was utilized to sample the Brillouin zone. To better determine the van der Waals (vdW) interactions, we employed the DFT + D3 correction.[6] The 2D FeN_4-SAzyme monolayer was placed in the xy plane with the z direction perpendicular to the layer plane, and a vacuum distance of ~15Å was employed to avoid the interaction between adjacent layers. To study the properties of the FeN_4-SAzyme layer, a 5 ×5 supercell was employed.

To estimate the ORR catalytic performance of our FeN_4-SAzyme monolayer, we computed the Gibbs free energy (ΔG) of each reaction step in ORR for acquiring the corresponding free energy profile using the computational electrode model (CHE).[7,8] On the basis of this model, the ΔG of each elementary step can be determined by: $\Delta G = \Delta E + \Delta ZPE - T\Delta S$, where ΔE can be directly determined from DFT computations.

ΔZPE refers to the change in zero-point energy, while ΔS denotes the energy difference of entropy, and T is the room temperature (298.15 K). Notably, the ZPE and S of oxygenated intermediates in ORR were obtained by computing their vibrational frequencies, while those of free H_2 and H_2O molecules were obtained from the NIST database. The potential of (H^++ e^-) in solution at standard conditions was assumed as the potential of 1/2 H_2. To simulate a strong acid environment in this work, pH = 0 was chosen, thus the contribution of free energy (ΔGpH) from H concentration will be neglected (ΔGpH = -kBTln10 × pH). The Gibbs free energy of O_2 (G_{O2}) was determined according to the following equation: G_{O2}= G_{H2O} - 2G_{H2} + 4.92 eV. After obtaining the ΔG values of each elementary step in ORR, the limiting potential (U_L) an be obtained: U_L = -max (ΔG_1, ΔG_2, ΔG_3, ΔG_4)/e, which has been widely-accepted as the descriptor for thermodynamically evaluating the catalytic performance of ORR on a given electrocatalyst.

Synthesis of FeN_4F-SAzyme, FeN_4Cl-SAzyme, FeN_4Br-SAzyme, FeN_4I-SAzyme.

16 g of melamine, 4 g of α-cellulose, 0.289 g of $Fe(NO_3)_3$ and 1 g of thiourea were added to the ball mill jar for 1.5 h. Subsequently, hydrofluoric acid (HF), hydrochloric acid (HCl), hydrobromic acid (HBr) and hydroiodic acid (HI) diluted with 3 mol/L ethanol were added to the ball mill jar, respectively. Then, 60 °C oven drying was performed and the dried powder was continued to be ball milled for 1.5 h. Subsequently, the powder was subjected to pyrolysis at temperature of 550 °C for 1 h with a heating rate of 2 °C/min and 1000 °C for 2 h with a heating rate of 2 °C/min. The

obtained product was add to 2 mol/L HNO_3 and 1 mol/L HCl in a water bath with 90 °C for 10 h. To make the Fe metal particles without coordination were removed. Then, the solution was extracted and dried. Finally, the sample were fixed by reheating in a tube furnace at 900 °C to obtain the final catalyst.

Experimental Material

Melamine ($C_3H_6N_6$, Aladdin, 99% purity), α-Cellulose (50 μm, Aladdin), Iron nitrate nonahydrate ($FeN_3O_9 \cdot 9H_2O$, Aladdin), Thiourea (CH_4N_2S, Aladdin), Hydrofluoric acid (Tianjin), Hydrochloric acid, Hydrobromic acid (Macklin), Hydroiodic acid (Macklin), Nitric acid, 20 wt.% commercial Pt/C (Hesen), Argon gas, Isopropyl Alcohol (C_3H_8O, 99.9% purity), Nafion117 solution (Aladdin).

Electrochemical Measurement

The catalyst ink was prepared by dissolve 5 mg of the black powder in 1 ml of solution with the ratio of isopropyl alcohol: water: nafion = 480 μL: 480 μL: 40 μL followed by perform sonication for 1 h. The obtained black homogeneous solution was dropped on the surface of the rotating disc electrode (RDE) and then dried naturally. Afterwards, the electrochemical properties were tested.

The catalyst performance was tested using a three-electrode system including a working electrode (rotating disk electrode), a counter electrode (carbon electrode) and a reference electrode (saturated calomel electrode) in oxygen-saturated 0.1 M KOH as the electrolyte. Cyclic voltammetry (CV) and linear sweep voltammetry (LSV) were measurements using a CHI 760E (Chenhua, Shanghai) electrochemical workstation to obtain the catalyst performance parameters.

Characterizations

The scanning electron microscope (SEM) was recorded using a EM-30plus with electron acceleration energy of 20 kV. TEM images were performed on a JEM-2100 transmission electron microscope with electron acceleration energy of 200 kV. AFM was tested by Multimode8. Raman spectra were carried out by DXR2. Structural and morphological information was obtained by X-ray diffraction (XRD-6100) with Cu Kα, λ = 1.5406 Å. XPS Photoelectric emission spectroscopy measurement was recorded by THERMO. Elemental analysis of Fe in the catalyst was detected by an avio200 inductively coupled plasma optical emission spectrometry (ICP-OES).

Koutecky-Levich equation:

$$\frac{1}{J}=\frac{1}{J_L}+\frac{1}{J_k}=\frac{1}{B\omega^{\frac{1}{2}}}+\frac{1}{J_k}$$

$$B=0.62nFC_0D_0^{2/3}V^{-1/6}$$

where J is the measured current density, J_κ and J_L are the kinetic and limiting current densities, ω is the angular velocity of the disk, n is the electron transfer number, F is the Faraday constant (96485 C·mol^{-1}), C_0 is the bulk concentration of O_2 (1.2 × 10^{-6} mol·cm^{-3}), D_0 is the diffusion coefficient of O_2 (1.9 × 10^{-5} cm^2·s^{-1}), and V is the kinematic viscosity of the electrolyte (0.01 cm^2·s^{-1}).

Tafel slopes were obtained according to the Tafel equation:

$$\eta = a + b \log j$$

where η was the overpotential, j was the measured current density, and b was the Tafel slope.

Electrochemically active surface areas (ECSA):

The ECSA of a material with similar composition is proportional to its electrochemical double-layer capacitance (C_{dl}), which was measured by CV in a non-Faradaic region at different scan rates (V_b) of 20, 40, 60, 80, and 100 mV s^{-1}. Then the double-layer capacitance (C_{dl}) was estimated by plotting the $\Delta j = (ja\text{-}jc)$ at 1.14 V vs. RHE as a function of the scan rate. It can be calculated using the equation:

$$C_{dl} = \frac{dl(\Delta j)}{2dl v_b}$$

The ECSA can be calculated from the C_{dl} according to:

$$ECSA = \frac{C_{dl}}{C_S}$$

Where Cs is the specific capacitance of a flat surface with 1 cm^2 of real surface area.

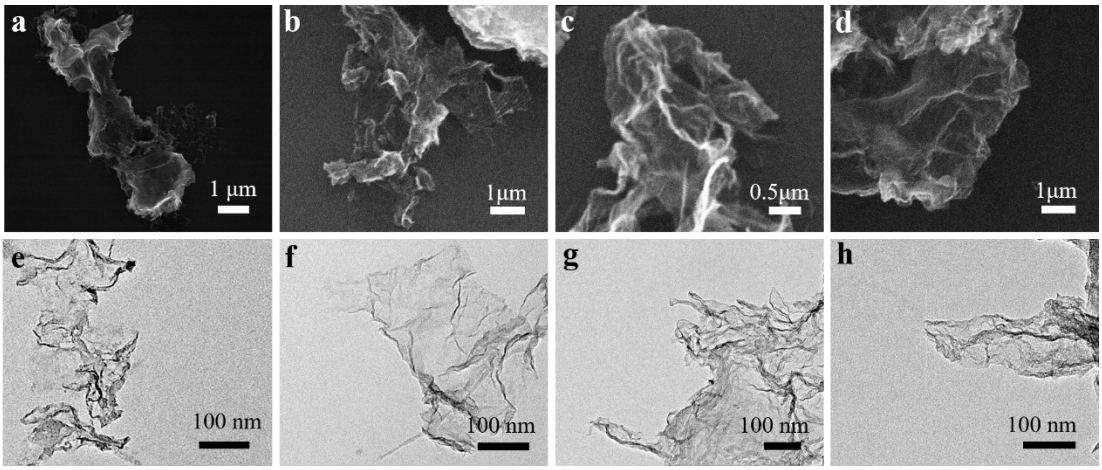

Fig. S1 The SEM image of (a) FeN_4-SAzyme, (b)FeN_4F-SAzyme, (c) FeN_4Br-SAzyme and (d) FeN_4I-SAzyme, respectively. The TEM image of (e) FeN_4-SAzyme (f) FeN_4F-SAzyme, (g) FeN_4Br-SAzyme and (h) FeN_4I-SAzyme, respectively.

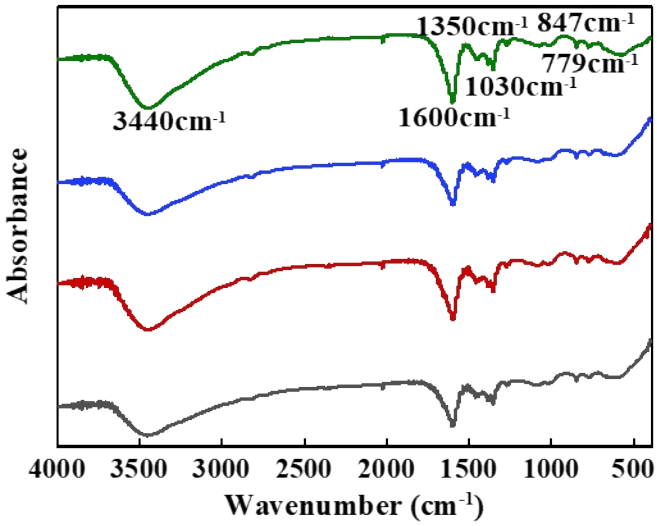

Fig. S2 FTIR spectrum of FeN_4F-SAzyme (green line), FeN_4Cl-SAzyme (blue line), FeN_4Br-SAzyme (red line) and FeN_4I-SAzyme (black line), respectively.

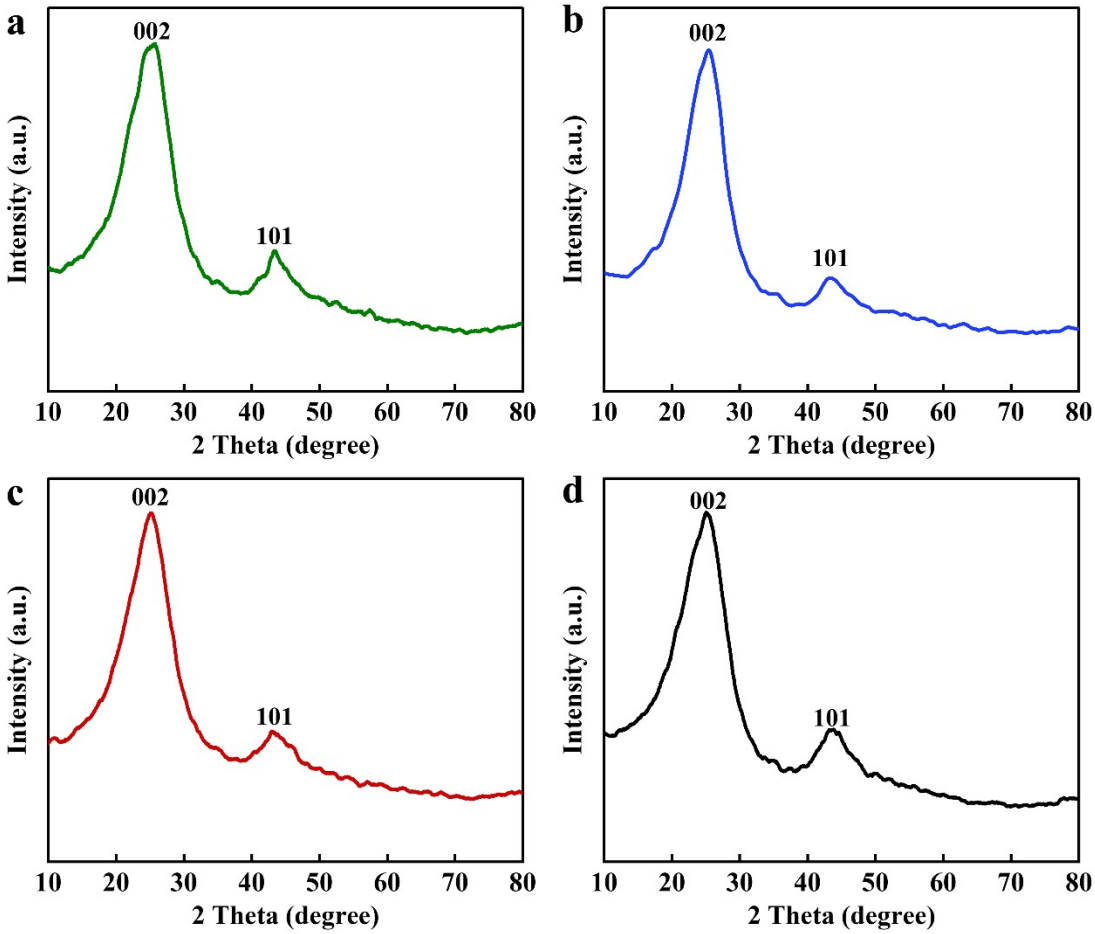

Fig. S3 XRD patterns of (a) FeN_4F-SAzyme (b) FeN_4Cl-SAzyme (c) FeN_4Br-SAzyme

and (d) FeN_4I-SAzyme.

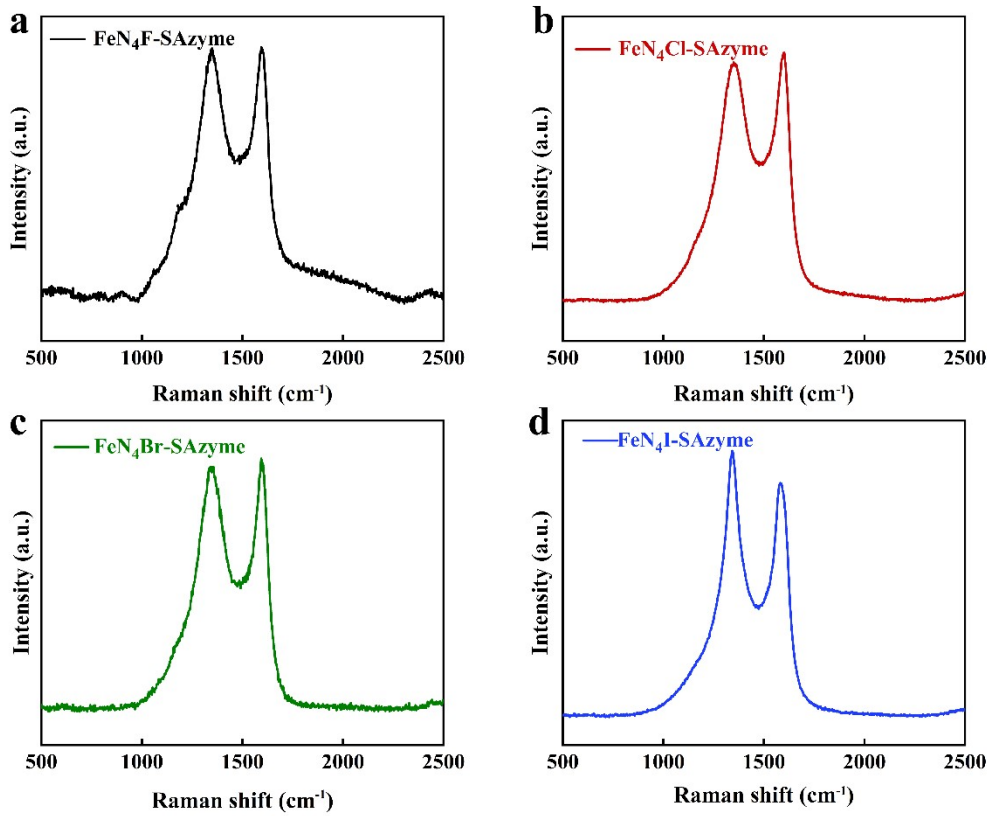

Fig. S4 Raman spectra of the (a) FeN_4F-SAzyme, (b) FeN_4Cl-SAzyme, (c) FeN_4Br-SAzyme and (d) FeN_4I-SAzyme.

FeN_4F-SAzyme	**FeN_4Cl-SAzyme**
I_D/I_G=0.9896	I_D/I_G=0.9561
FeN_4Br-SAzyme	**FeN_4I-SAzyme**
I_D/I_G=1.0000	I_D/I_G=1.1366

Table 1. The I_D/I_G of FeN_4F-SAzyme, FeN_4Cl-SAzyme, FeN_4Br-SAzyme, FeN_4I-SAzyme, respectively.

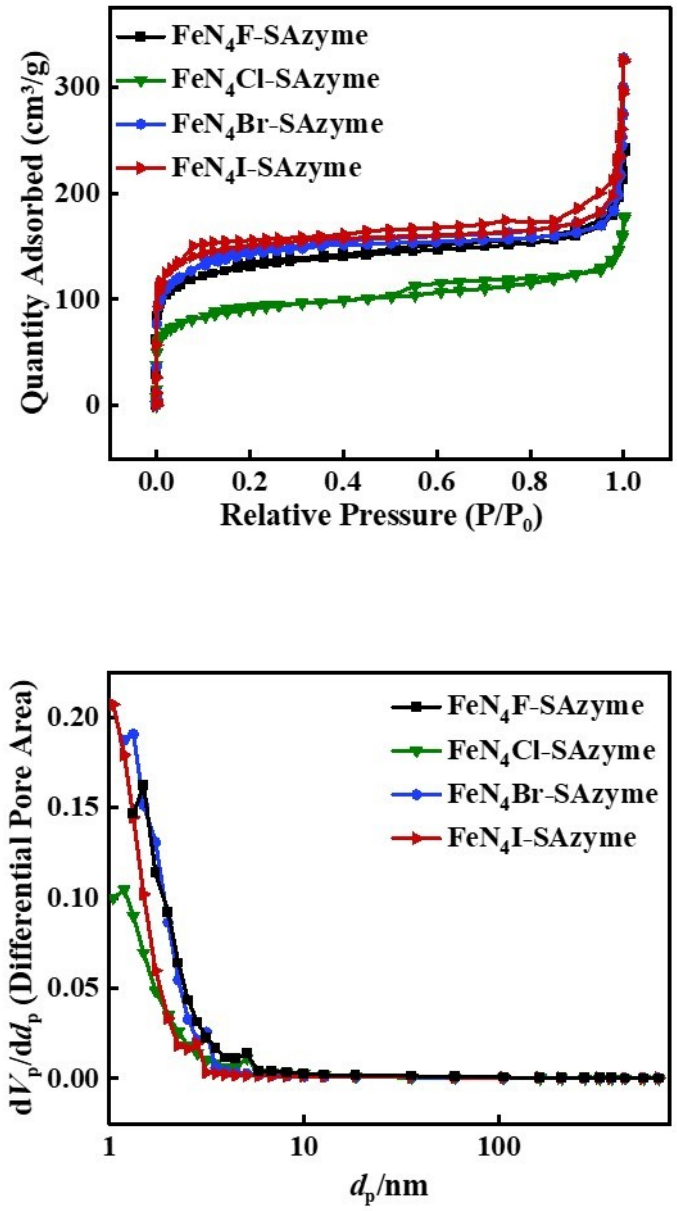

Fig. S5 N_2 adsorption-desorption isotherms and the corresponding pore size distribution of FeN_4F-SAzyme, FeN_4Cl-SAzyme, FeN_4Br-SAzyme, FeN_4I-SAzyme.

	BET(m^2 g^{-1})	Pore diameter
FeN_4F-SAzyme	480.47	2.5524
FeN_4Cl-SAzyme	333.87	2.8084
FeN_4Br-SAzyme	526.34	2.7654
FeN_4I-SAzyme	564.73	3.0940

Table 2. The BET and Pore diameter of FeN_4F-SAzyme, FeN_4Cl-SAzyme, FeN_4Br-SAzyme, FeN_4I-SAzyme, respectively.

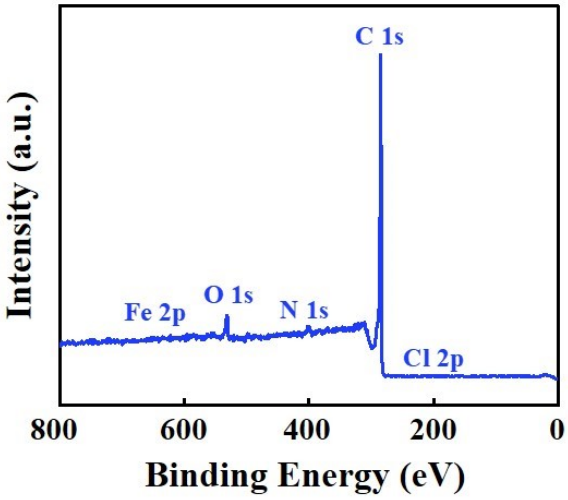

Fig. S6 The survey spectrum of FeN_4Cl-SAzyme.

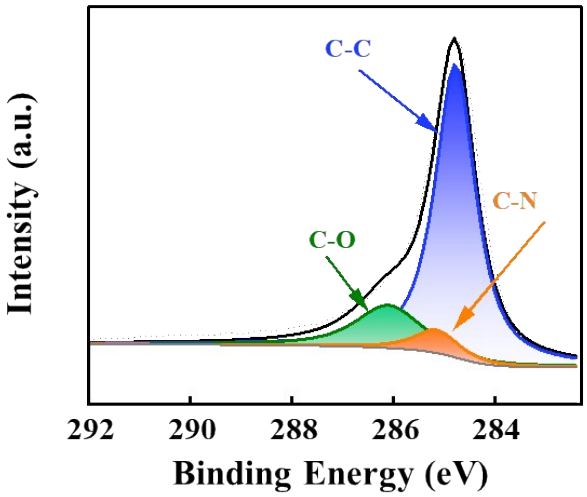

Fig. S7 The C 1s district of FeN_4Cl-SAzyme.

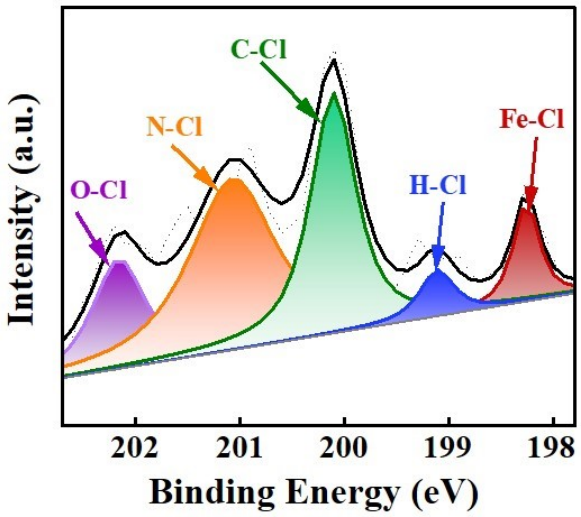

Fig. S8 The Cl 2p district of FeN_4Cl-SAzyme.

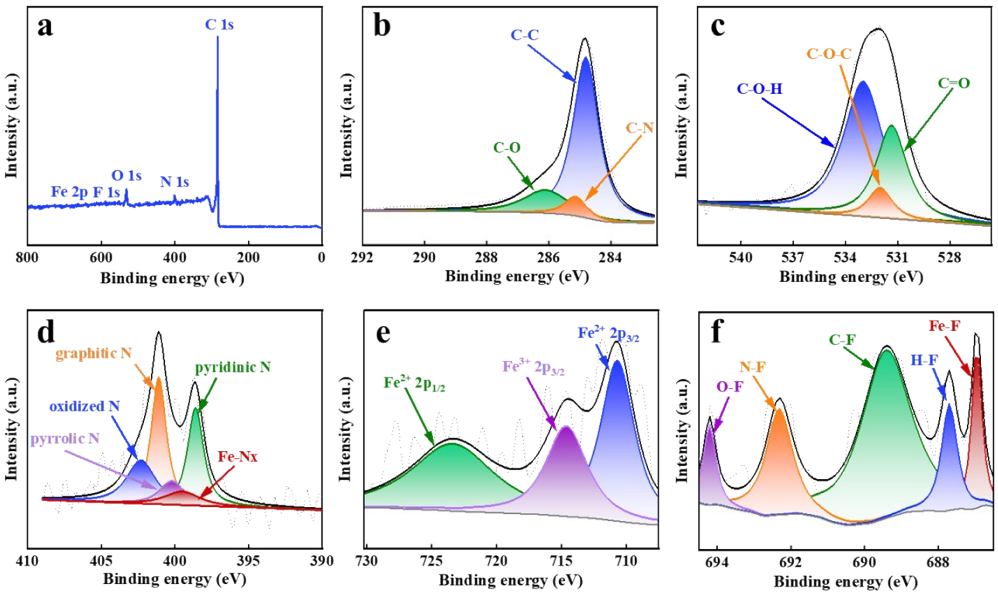

Fig. S9 XPS spectroscopy analysis of catalyst (a) survey spectrum (b) the C 1s (c) the O 1s (d) the N 1s (e) the Fe 2p and (f) the Cl 2p district of FeN_4F-SAzyme.

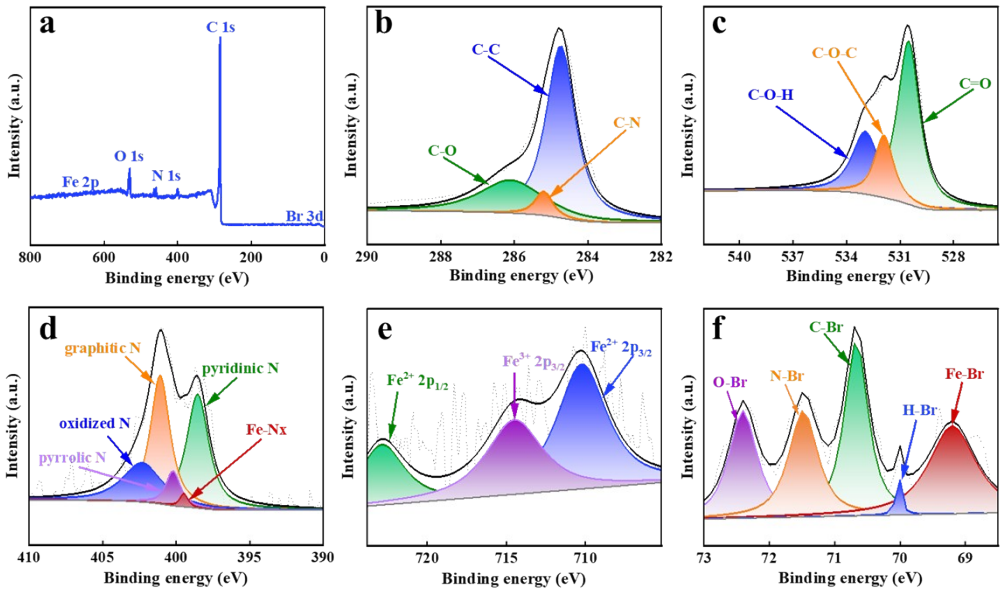

Fig. S10 XPS spectroscopy analysis of catalyst (a) survey spectrum (b) the C 1s (c) the O 1s (d) the N 1s (e) the Fe 2p and (f) the Cl 2p district of FeN_4Br-SAzyme.

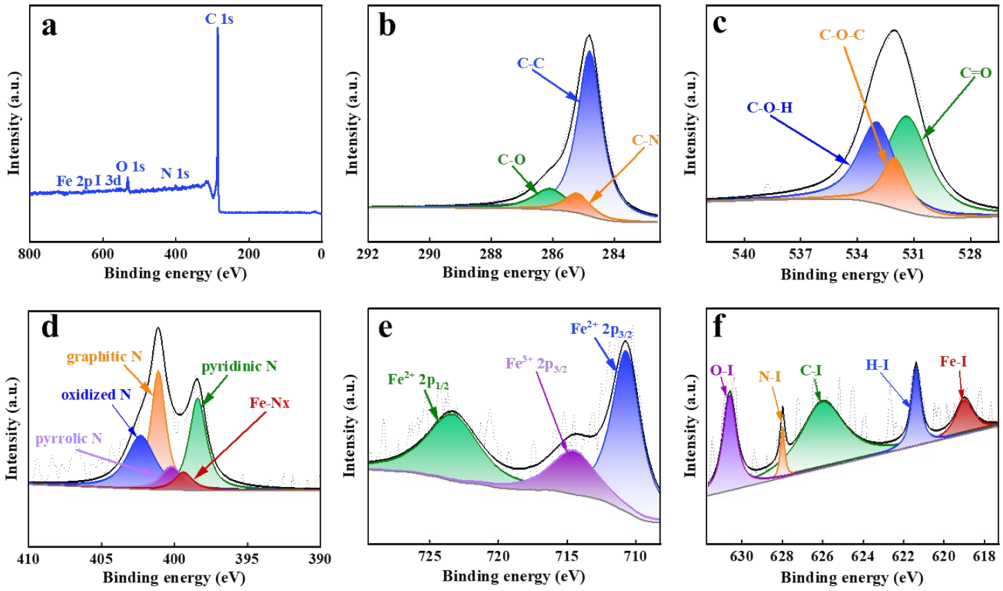

Fig. S11 XPS spectroscopy analysis of catalyst (a) survey spectrum (b) the C 1s (c) the O 1s (d) the N 1s (e) the Fe 2p and (f) the Cl 2p district of FeN_4I-SAzyme.

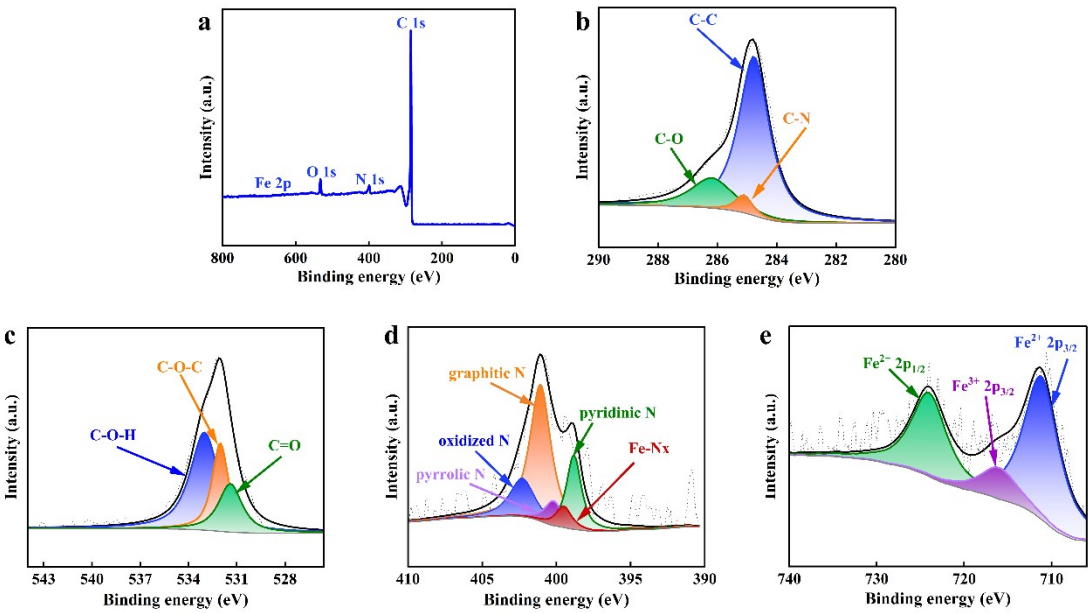

Fig. S12 XPS spectroscopy analysis of catalyst (a) survey spectrum (b) the C 1s (c) the O 1s (d) the N 1s and (e) the Fe 2p district of FeN_4-SAzyme.

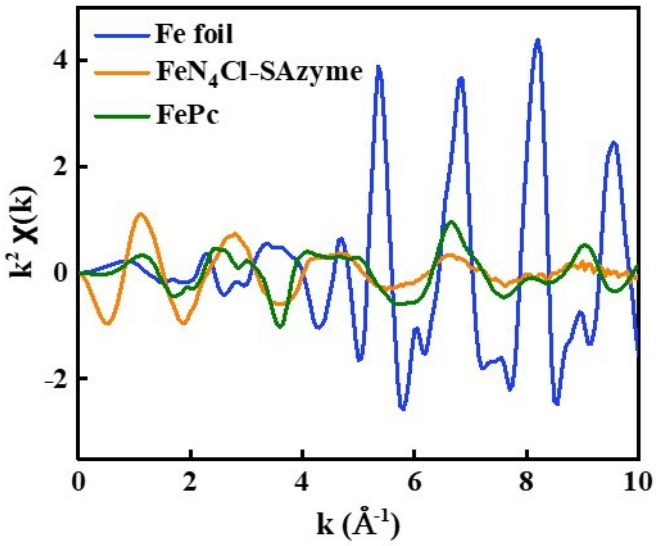

Fig. S13 Fe *K*-edge EXAFS for Fe foil, FePc and FeN_4Cl-SAzyme, shown in k^2-weighted k-space.

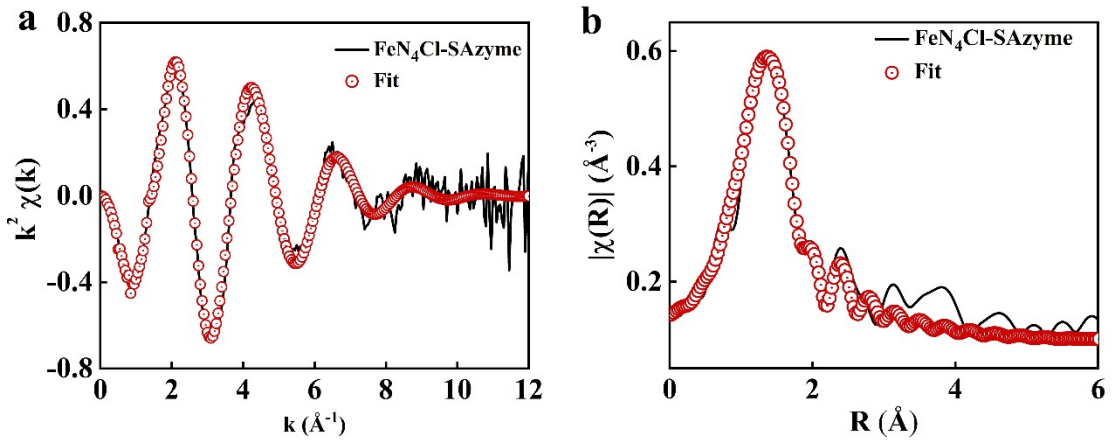

Fig. S14 EXAFS fitting curves of FeN4Cl-SAzyme in (a) k space and (b) R space.

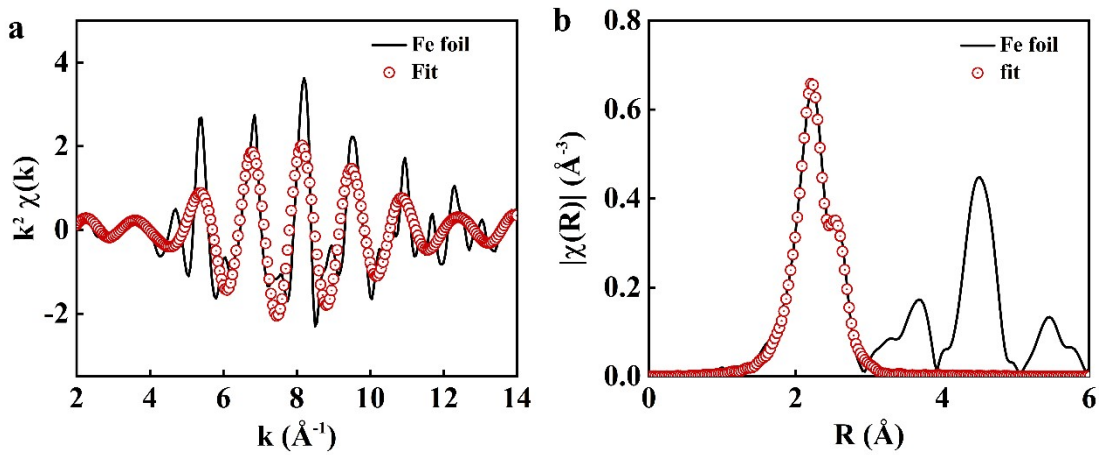

Fig. S15 EXAFS fitting curves of FeN4Cl-SAzyme in (a) k space and (b) R space.

Sample	Scattering Pair	CN	R (Å)	σ^2	ΔE_0 (eV)	R factor
FeN_4Cl-SAzyme	Fe-N	4.4	1.93	0.00105	7.467	0.01203
	Fe-Cl	1.2	2.37	0.00182		
Fe foil	$Fe-Fe_1$	8	2.48	0.00278	8.371	0.00695
	$Fe-Fe_2$	6	2.86	0.00370		

Table 3. Structural parameters of FeN_4Cl-SAzyme extracted from the EXAFS fitting. CN is the coordination number, R is interatomic distance; σ^2 is DebyeWaller factor (a measure of thermal and static disorder in absorber-scatterer distances); ΔE_0 is edge-energy shift (the difference between the zero kinetic energy value of the sample and that of the theoretical model). R factor is used to value the goodness of the fitting.

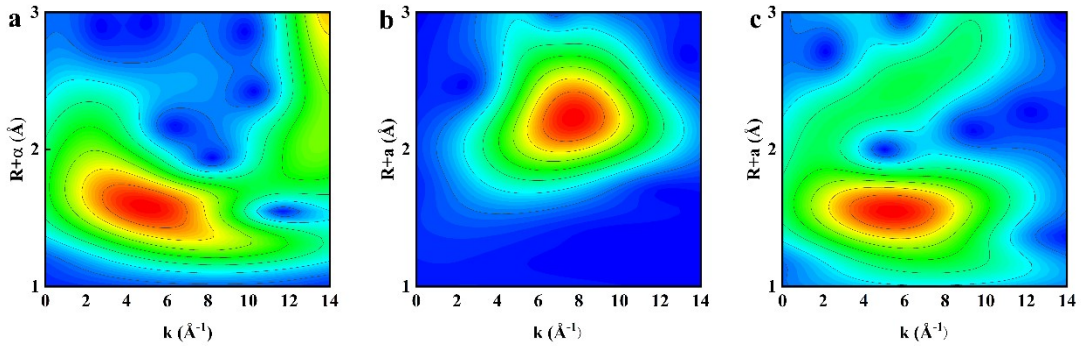

Fig. S16 WT contour plots of (a) FeN_4Cl-SAzyme in comparison with (b) Fe foil and (c) FePc samples.

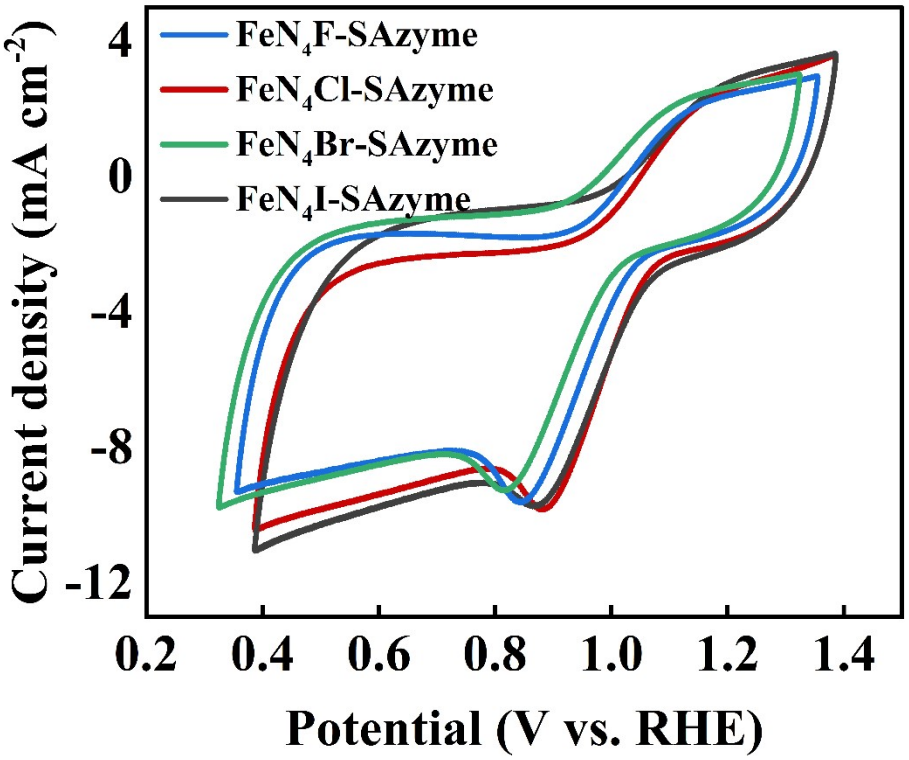

Fig. S17 Cyclic voltammograms with the FeN_4F-SAzyme, FeN_4Cl-SAzyme, FeN_4Br-SAzyme, FeN_4I-SAzyme in O_2-saturated 0.1 M KOH.

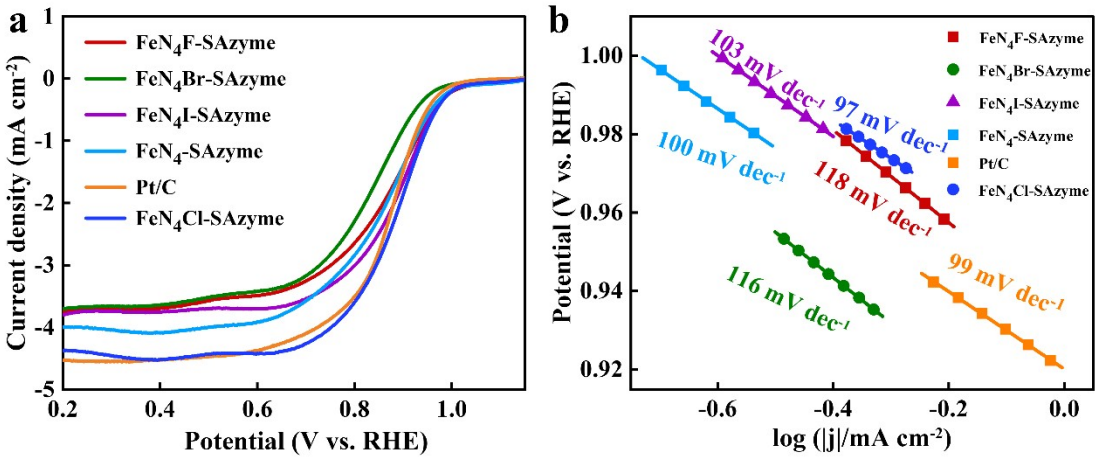

Fig. S18 The (a) linear sweep voltammetry (LSV) curves of FeN_4F-SAzyme, FeN_4Cl-SAzyme, FeN_4Br-SAzyme, FeN_4I-SAzyme, Pt/C and FeN_4-SAzyme (b) The tafel slope of FeN_4F-SAzyme, FeN_4Cl-SAzyme, FeN_4Br-SAzyme, FeN_4I-SAzyme, Pt/C and FeN_4-SAzyme.

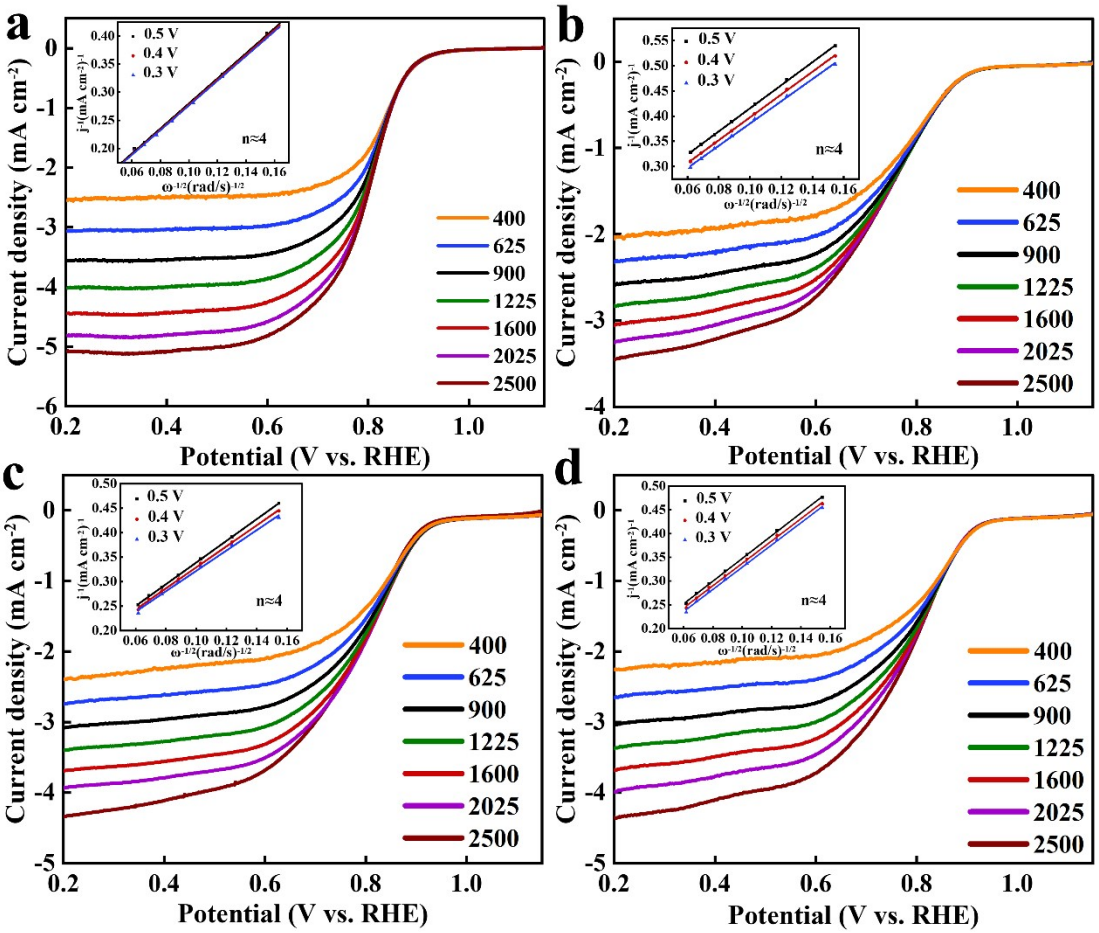

Fig. S19 LSV scans with different rotational speeds of (a) Pt/C, (b) FeN_4F-SAzyme, (c) FeN_4Br-SAzyme and (d) FeN_4I-SAzyme.

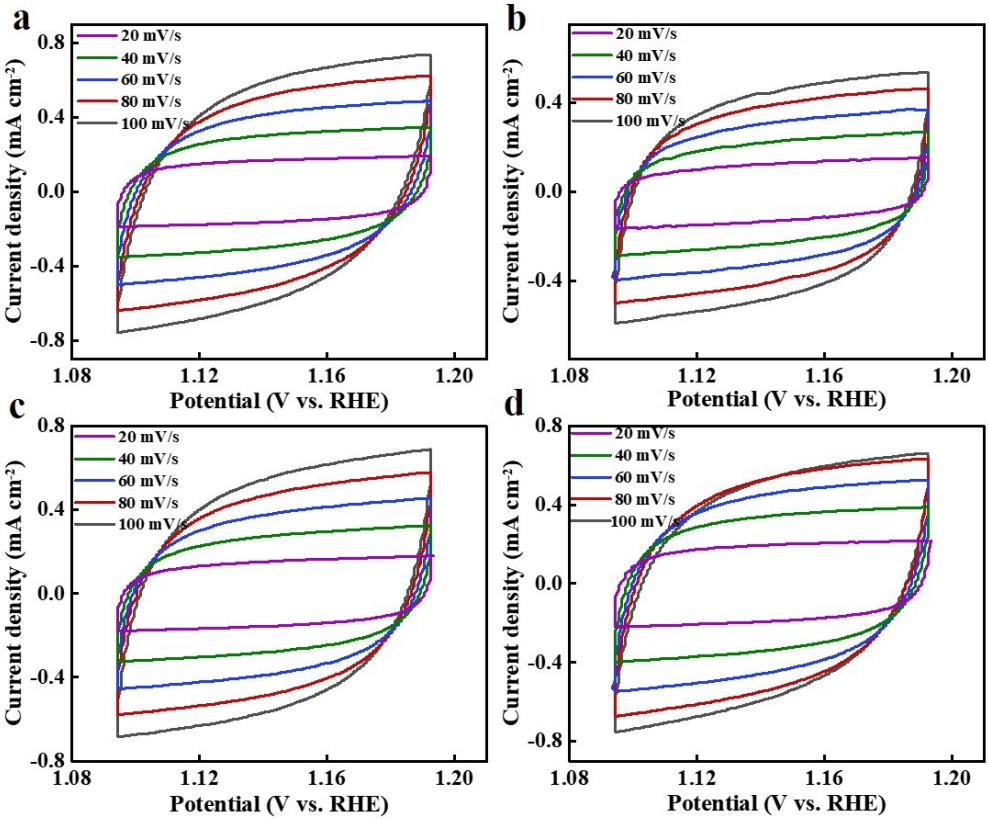

Fig. S20 CV curves of (a) FeN_4F-SAzyme, (b) FeN_4Cl-SAzyme, (c) FeN_4Br-SAzyme and (d) FeN_4I-SAzyme at 100 mV s^{-1}, 80 mV s^{-1}, 60 mV s^{-1}, 40 mV s^{-1} and 20 mV s^{-1}, respectively.

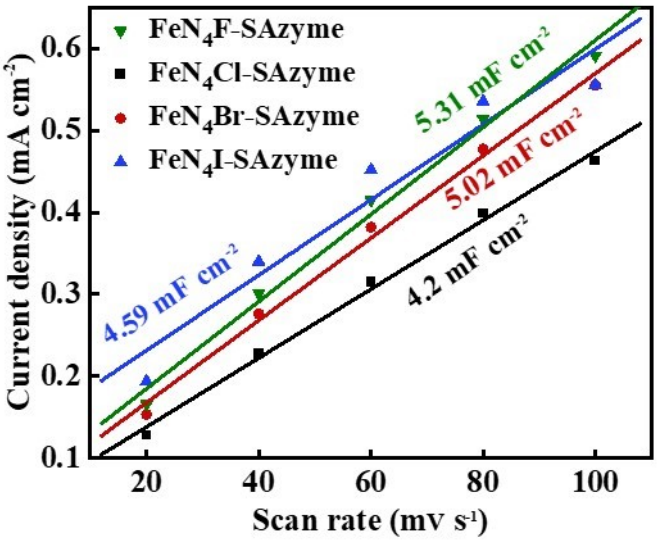

Fig. S21 Electrical double-layer capacitor of FeN_4F-SAzyme, FeN_4Cl-SAzyme, FeN_4Br-SAzyme and FeN_4I-SAzyme, respectively.

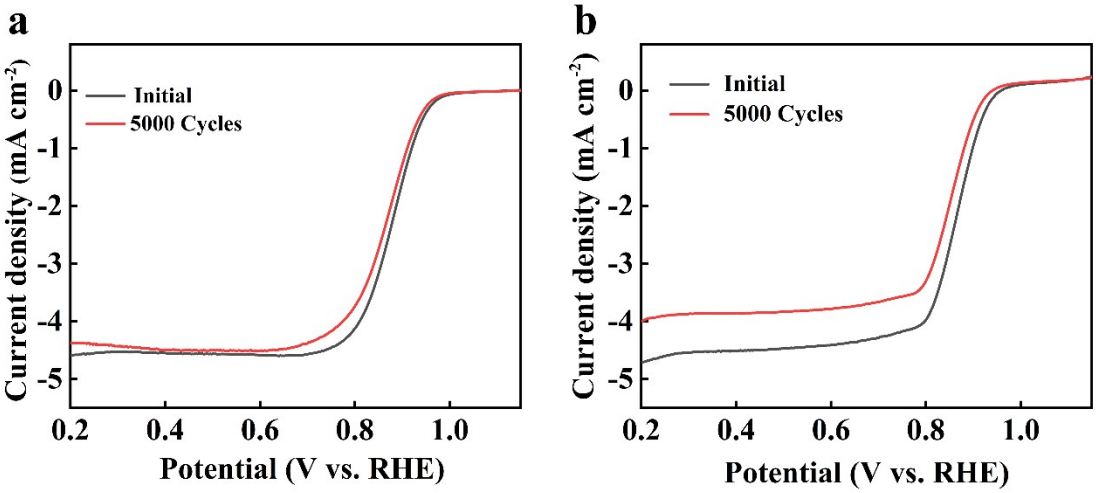

Fig. S22 The ORR polarization curves before and after 5000 for (a) FeN_4Cl-SAzyme and (b) Pt/C in 0.1 M KOH.

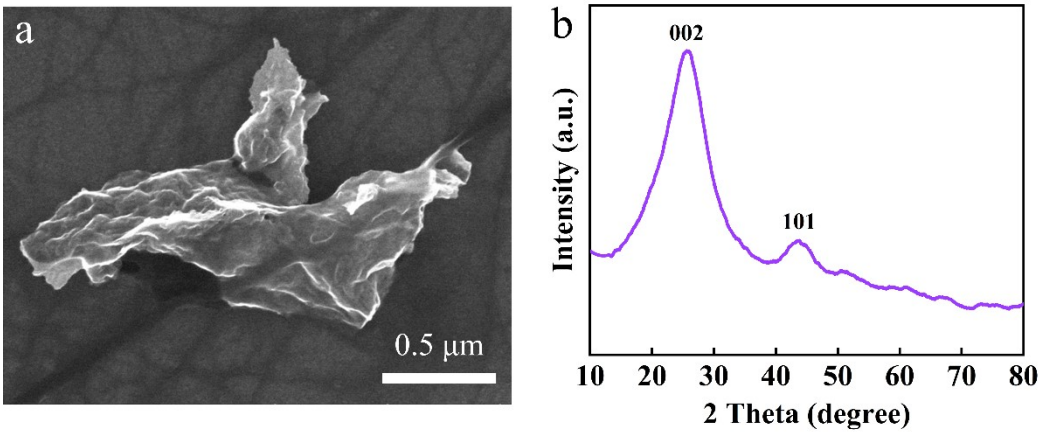

Fig. S23 The (a) SEM and (b) XRD of FeN4Cl-SAzyme after long-term testing.

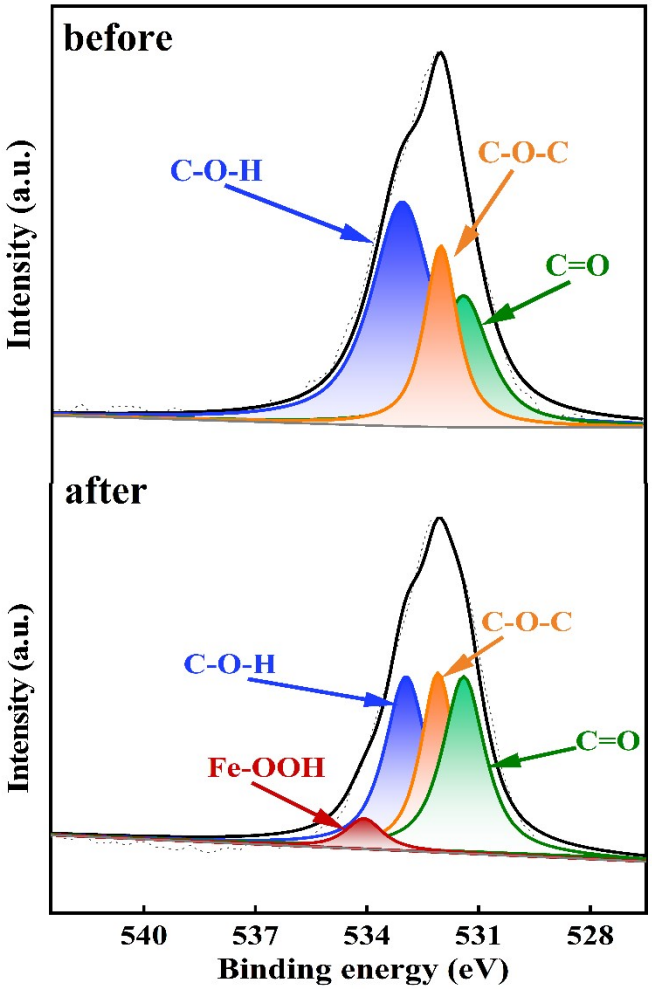

Fig. S24 O-spectrum test before and after the reaction of FeN_4F-SAzyme.

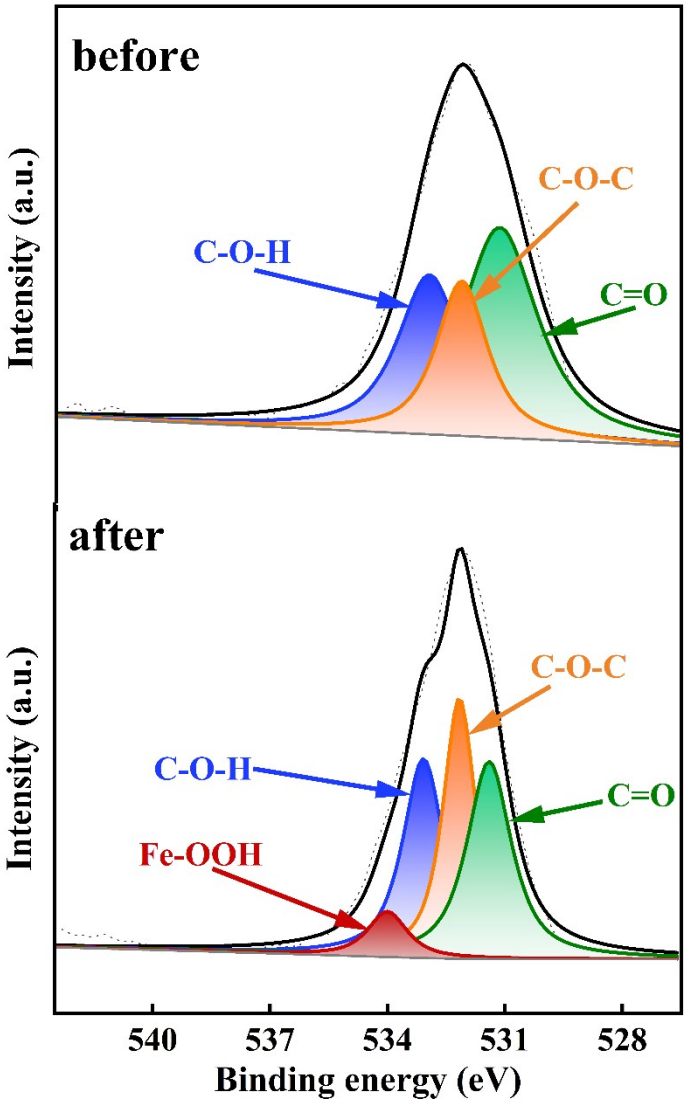

Fig. S25 O-spectrum test before and after the reaction of FeN_4Br-SAzyme.

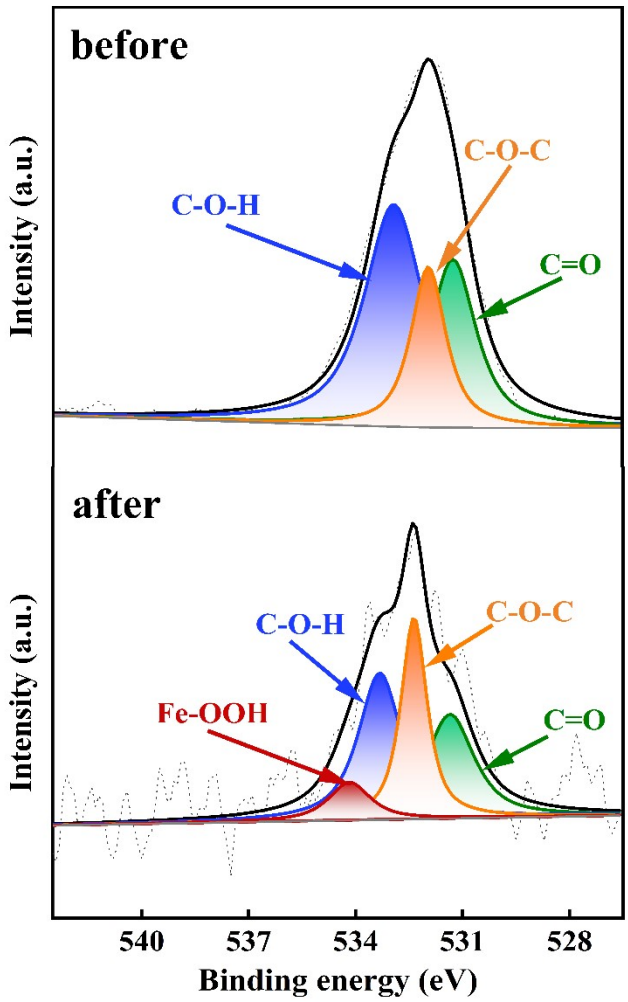

Fig. S26 O-spectrum test before and after the reaction of FeN_4I-SAzyme.

	Area (Fe-O)	Area (C-O-H)	Area (C-O-C)	Area (C=O)
FeN_4F-SAzyme	1970.196	13100.16	10928.63	13214.03
FeN_4Cl-SAzyme	2432.726	6979.023	5667.365	5784.839
FeN_4Br-SAzyme	189.5074	758.8887	631.0668	602.2238
FeN_4I-SAzyme	2993.394	13767.13	14284.14	14693.8

Table 4. The area (Fe-O, C-O-H, C-O-C, C=O) of FeN_4F-SAzyme, FeN_4Cl-SAzyme, FeN_4Br-SAzyme and FeN_4I-SAzyme, respectively.

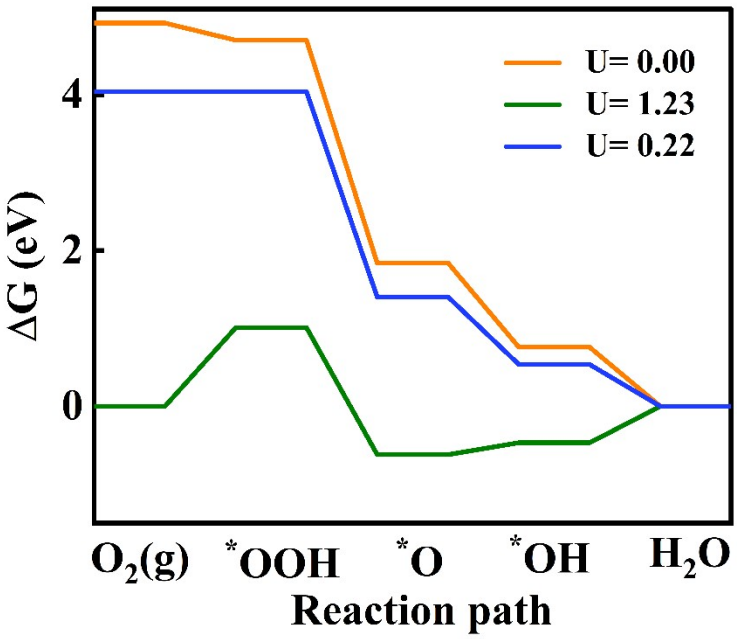

Fig. S27 Calculated gibbs free energy diagrams of $4e^-$ ORR pathway on FeN_4F-SAzyme.

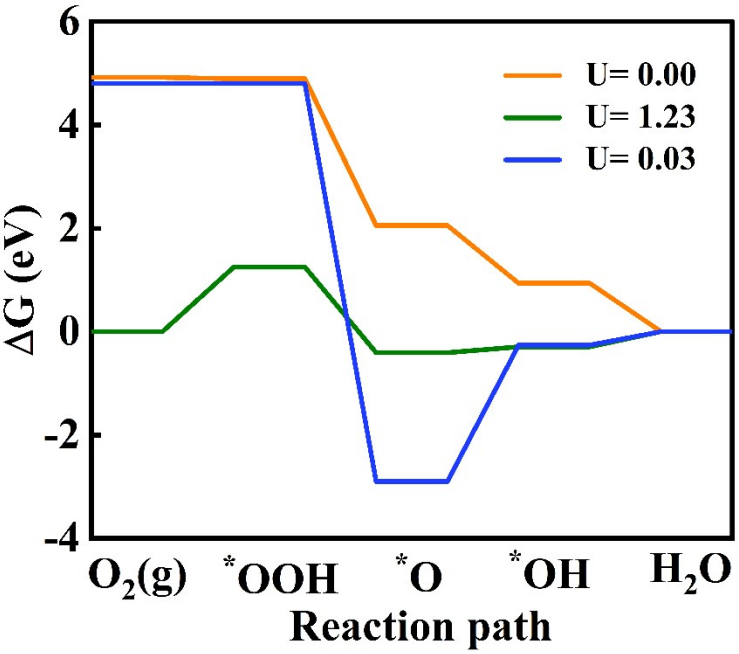

Fig. S28 Calculated gibbs free energy diagrams of $4e^-$ ORR pathway on FeN_4Br-SAzyme.

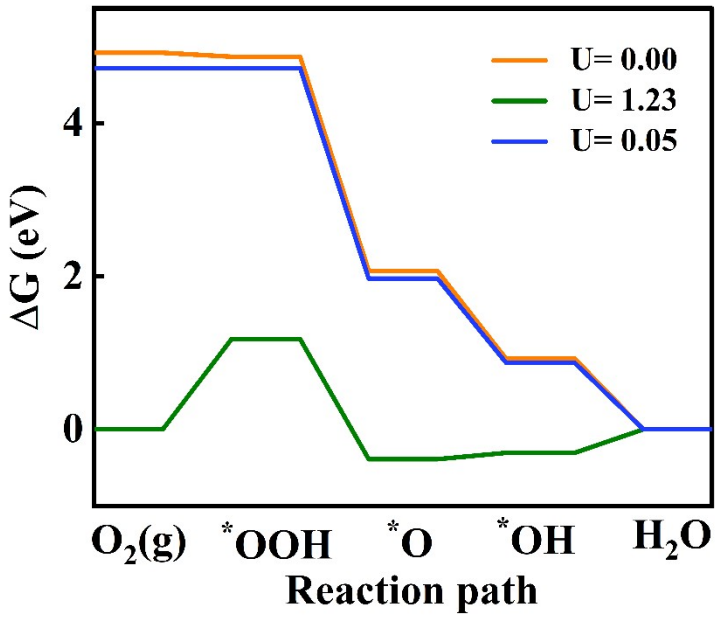

Fig. S29 Calculated gibbs free energy diagrams of $4e^-$ ORR pathway on FeN_4I-SAzyme.

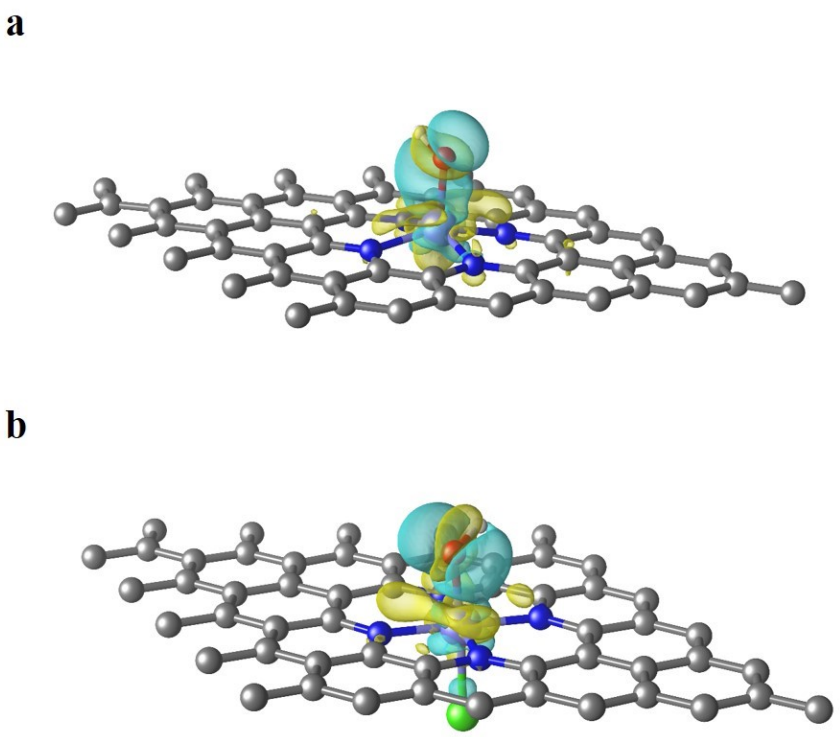

Fig. S30 The charge density difference of FeN_4-SAzyme (a) and FeN_4Cl-SAzyme (b) with O* adsorption from a 3-dimensional view.

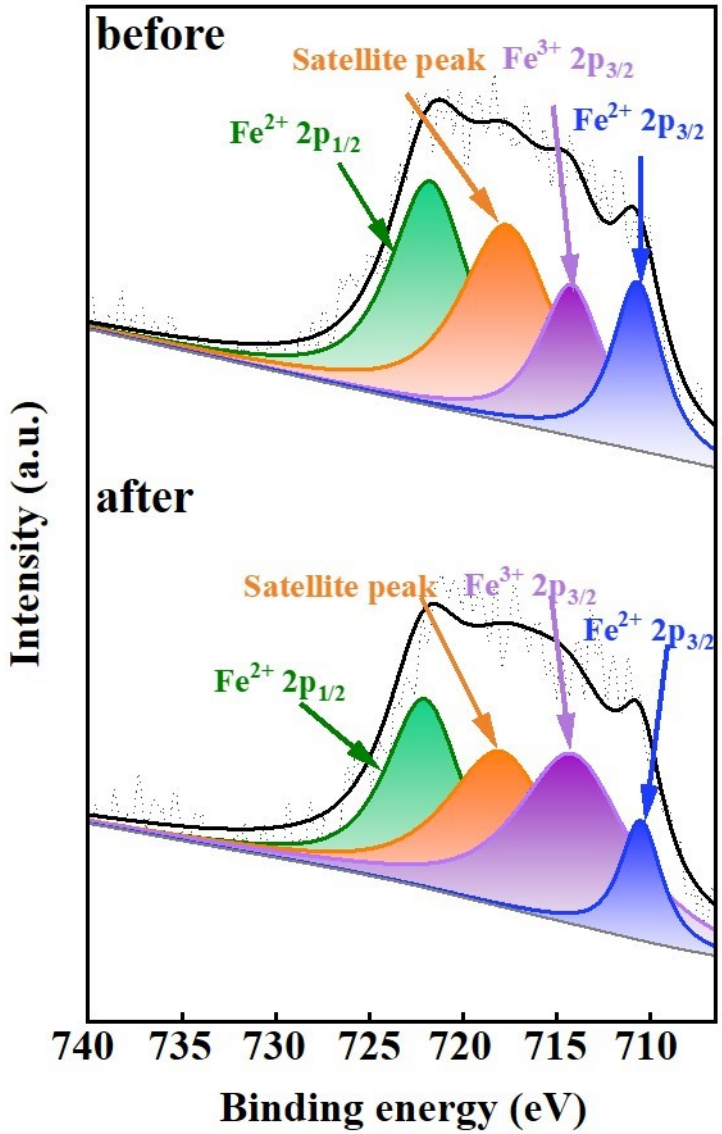

Fig. S31 Fe-spectrum test before and after the reaction of FeN_4F-SAzyme.

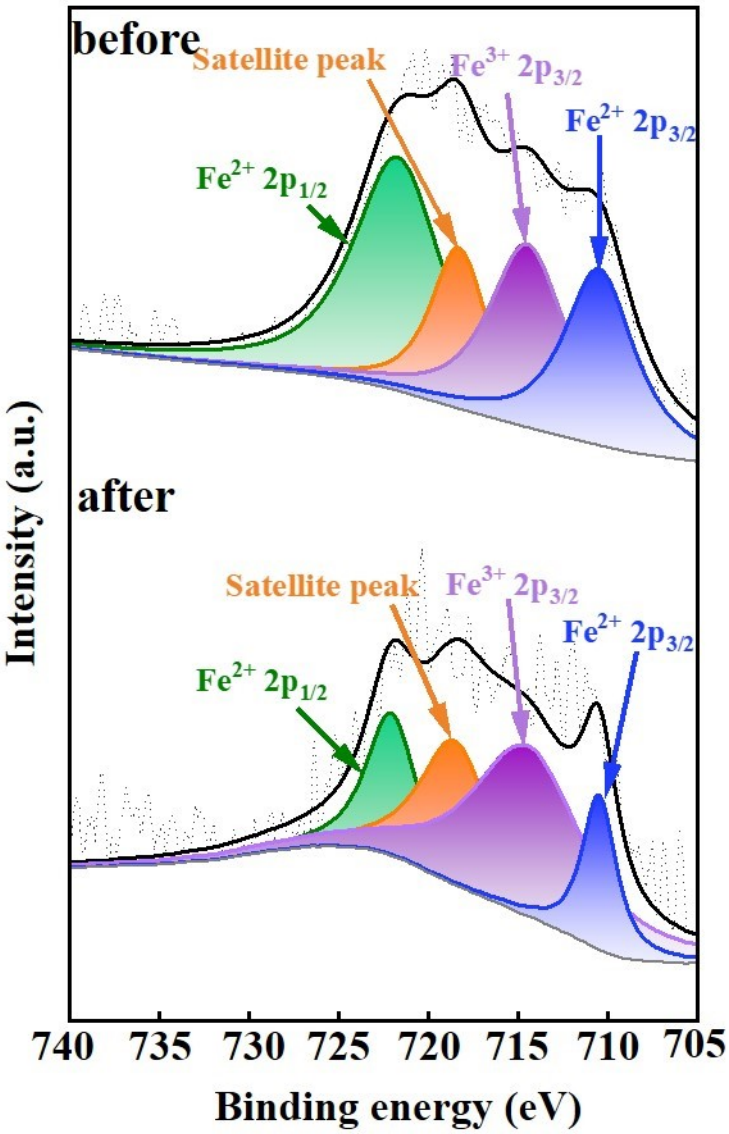

Fig. S32 Fe-spectrum test before and after the reaction of FeN_4Cl-SAzyme.

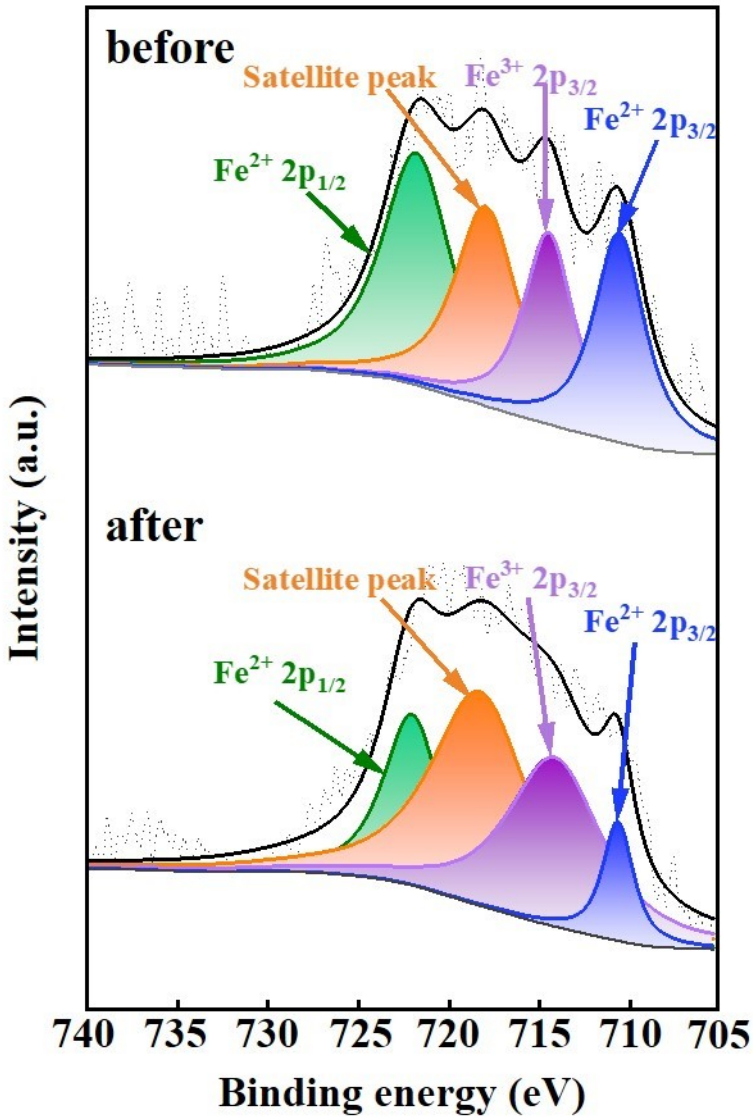

Fig. S33 Fe-spectrum test before and after the reaction of FeN_4Br-SAzyme.

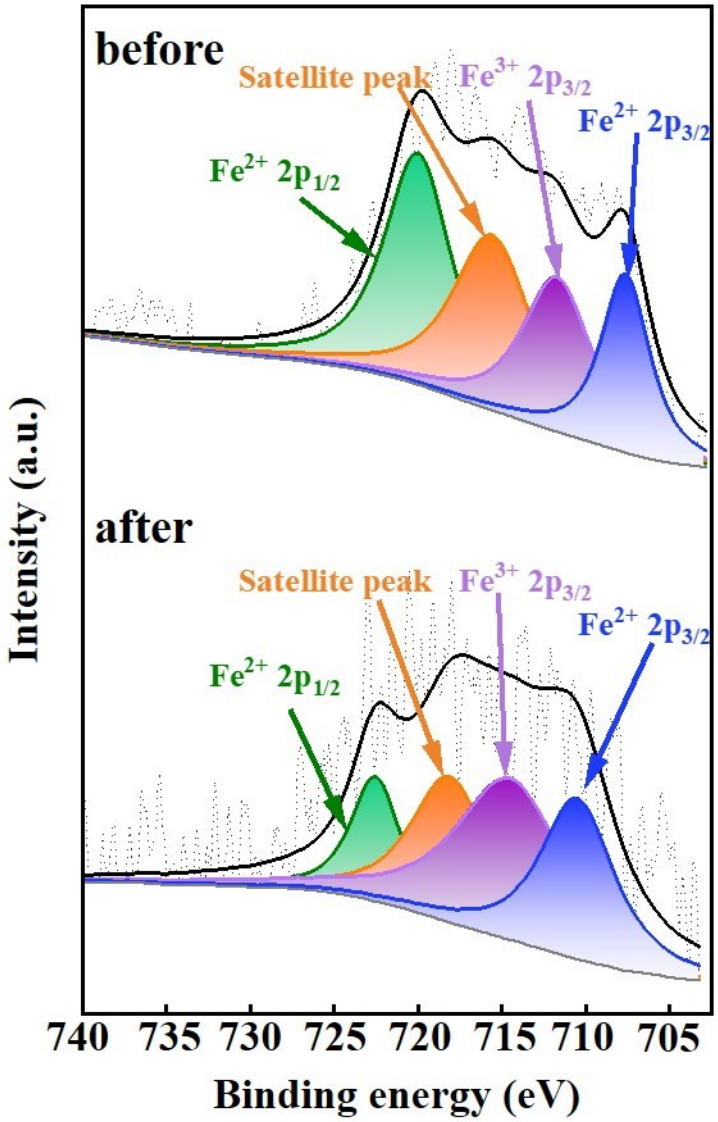

Fig. S34 Fe-spectrum test before and after the reaction of FeN_4I-SAzyme.

	Area (Fe^{2+} $2p_{3/2}$)	Area (Fe^{3+} $2p_{3/2}$)	Area (Fe^{2+} $2p_{1/2}$)
FeN_4F-SAzyme (before)	1878.251	2179.639	4056.667
FeN_4F-SAzyme (after)	1365.49	5265.104	4100.177
FeN_4Cl-SAzyme	7180.536	8294.58	12203.52

(before)			
FeN_4Cl-SAzyme (after)	1851.969	6585.678	2500.341
FeN_4Br-SAzyme (before)	3743.709	3437.806	5670.871
FeN_4Br-SAzyme (after)	2329.944	10102.06	6212.925
FeN_4I-SAzyme (before)	4099.982	5077.203	7430.271
FeN_4I-SAzyme (after)	2349.763	3524.603	1231.35

Table 5. The area (Fe^{2+} $2p_{3/2}$, Fe^{3+} $2p_{3/2}$, Fe^{2+} $2p_{1/2}$) of FeN_4F-SAzyme, FeN_4Cl-SAzyme, FeN_4Br-SAzyme and FeN_4I-SAzyme at the before and after reaction, respectively.

References

1. G. Kresse and J. Hafner, *Phys. Rev., B Condens. Matter*, 1993, **47**, 558-561.

2. G. Kresse and J. Furthmüller, *Phys. Rev. B*, 1996, **54**, 11169.

3. P. E. Blochl, *Phys. Rev., B Condens. Matter*, 1994, **50**, 17953-17979.

4. G. Kresse and D. Joubert, *Phys. Rev. B*, 1999, **59**, 1758.

5. J. P. Perdew, K. Burke and M. Ernzerhof, *Phys. Rev. Lett*, 1996, **77**, 3865.

6. S. Grimme, *J. Comput. Chem*, 2006, **27**, 1787-1799.

7. J. Zhang, Z. Zhou, F. Wang, Y. Li and Y. Jing, *ACS Sustain. Chem. Eng.*, 2020, **8**, 7472-7479.

8. J. K. Nørskov, J. Rossmeisl, A. Logadottir, L. Lindqvist, J. R. Kitchin, T. Bligaard and H. Jonsson, *J. Phys. Chem. B*, 2004, **108**, 17886-17892.